# Development of nonstationary side forces along a slender body of revolution at incidence

D. Degani *
*Technion–Israel Institute of Technology, Haifa 32000, Israel*

(Received 18 August 2022; accepted 14 November 2022; published 12 December 2022)

The evolution of nonstationary side forces acting upon an axisymmetric ogive-cylinder body with a blunt base and subjected to flows at a wide range of angles of attack is studied numerically. To analyze the results, the body surface is divided into narrow cross-section disks and for each disk the time histories of rms and the mean of the side force are calculated and used to create bifurcation diagrams for angles of attack from 20° to 80°. These diagrams are compared with the diagrams obtained for the resultant side force acting on the entire body and those obtained for the ogive forebody and the cylindrical afterbody and its base. Results show that at low or medium angles of attack the flow is steady along the entire body except for some small oscillations near the body base. As the angle of attack increases beyond 40°, the flow about the aft of the cylindrical afterbody becomes unsteady and the side force oscillates with nonzero mean; this unsteady region extends upstream toward the nose as the angle of attack increases. When the angle of attack exceeds 50° the side force along the far aft of the body oscillates symmetrically with zero mean, and this symmetric region extends upstream with the increasing angle of attack until at $\alpha = 80°$ it stretches virtually over the entire body.

DOI: 10.1103/PhysRevFluids.7.124101

## I. INTRODUCTION

The flow about slender bodies of revolution becomes asymmetric with respect to the angle of attack plane, at a sufficiently high angle of attack. The first studies acknowledging the existence of vortex asymmetry of such flows, and consequently, the existence of aerodynamic side forces acting on the body, were published as early as the middle of the last century (e.g., Allen and Perkins [1], Letko [2], Gowen and Perkins [3,4], and Jorgensen and Perkins [5]). Over the years, the mystery of the unexplained cause of this asymmetry (and the potential practical benefit of an answer) has attracted many researchers and numerous studies have been published. Nevertheless, as of today, there is no satisfactory unified theory for the phenomenon. Most of the early studies were experiments (e.g., Gowen and Perkins [4], Thomson and Morrison [6], Lamont and Hunt [7], Lamont [8], Degani and Zilliac [9], Zilliac *et al.* [10], and Degani and Tobak [11]) focusing on several different aspects of the phenomenon.

The main difficulty the experimentalists faced was the sensitivity of the usually unstable flow to interferences caused by the supporting structure and by the measuring instruments: pitot tubes, hot-wire probes, or even surface pressure orifices. It is expected that the flow over a long circular cylinder perpendicular or highly inclined to the flow is unsteady if the Reynolds number is sufficiently high. It is also expected that for a finite-length cylinder, the shape of its ends should have a significant effect on the unsteady wake (e.g., Gowen and Perkins [4], Ramberg [12]). Nevertheless, most experimental studies of flows over slender bodies at high angles of attack have reported only the

*degani@technion.ac.il

 ©2022 American Physical Society

mean component of forces (e.g., Lamont and Hunt [7], Lamont [8,14], Zilliac *et al.* [10], Degani and Tobak [11,13], and Dexter and Hunt [15]). Few studies focused on specific types of unsteadiness; Degani and Zilliac [9] experimented with a pointed ogive-cylinder body of 3.5$D$ forebody and 12.5$D$ afterbody (where $D$ is the body diameter) and reported three types of unsteadiness in the wake: large-scale von Kármán vortex shedding, high-frequency pressure and velocity fluctuations indicative of the presence of free shear-layer vortices, and vortex interaction of the parallel shedding from the afterbody and the inclined vortices departing from the forebody. Ma *et al.* [16] measured flow unsteadiness over a short ogive-cylinder body ($L/D = 8$; $L$ is the body length) where the angle of attack ranges from $\alpha = 55^\circ$ to $\alpha = 85^\circ$. Using a pressure-measurement ring around the forebody at $x/D = 2.5$ ($x$ is the longitudinal axis with origin at the tip of the body), the distributed pressure measured was integrated to obtain sectional side forces. The results showed that at angles of attack $\alpha$ between $\alpha = 60^\circ$ and $\alpha = 80^\circ$ the flow was unsteady, fluctuating at low frequencies with large side-force amplitudes. The dominant frequency (Strouhal number between 0.038 and 0.072) was far less than the expected von Kármán vortex shedding frequency for this angle of attack range (i.e., Strouhal numbers between 0.15 and 0.20). Ma and Liu [17] simulated numerically the flow around a long ogive-cylinder body ($L/D = 22$) at two angles of attack; at $\alpha = 70^\circ$ they found that low-frequency (of Strouhal number St $= 0.054$) and high-amplitude fluctuation exist at $x/D < 5$. The frequency increases sharply at $x/D = 5$, and at $x/D > 5$ the frequencies were in the range of St $= 0.12$-$0.17$. The rms of the side force, Cy, reaches its maximum at about $x/D = 0.8$ (Cy $= 1.1$) and drops sharply to Cy $= 0.5$ at $x/D = 2.5$. For the rest of the body, the rms of the side-force coefficient Cy goes down monotonically to almost zero at the base of the body ($x/D = 22$). At $\alpha = 50^\circ$, fluctuations started only at $x/D = 2.5$ and then the rms of Cy grows monotonically from this point and down the body to reach a plateau of rms of Cy $\approx 1.4$ at $x/D = 12$. These aft results should be influenced by the wake at the base but the authors did not explain how the base was treated.

Experimental as well as computational studies have used many different slender body configurations but none of them had methodically checked the influence of the body length and its base on the side-force distribution. Most of the attention was given to the shape, fineness, and tip bluntness of the forebody (e.g., Gowen and Perkins [3], Thomson and Morrison [6], and Kruse *et al.* [18]); attention also was given to symmetry alternations of the forebody tip (Zilliac *et al.* [10], Degani and Tobak [11], Moskovitz *et al.* [19], Kumar [20], and Lua *et al.* [21]). Many added roughness or perturbations (Letko [2], Degani and co-workers [11,22,23], Ma *et al.* [24], Kumar and Prasad [25], Qi *et al.* [26], and Zhu *et al.* [27]). Some have dealt with the effect of the body base (e.g., Gowen and Perkins [3], and Ishay *et al.* [28]). A long, pointed slender body at a high angle of attack can be difficult to experiment with due to vibrations caused by the unsteady wake, and stiffening the support to overcome the problem increases its size and its adverse effect on the flow; many experimental studies brought up this issue (e.g., Lamont [8], Degani and Zilliac [9], Perkins [29], and Hunt and Dexter [30]). As a result, most of the models used in the experimental studies were short ($L/D = 10$ or less); consequently, most of the computational studies also used short bodies. Hence, the influence of the afterbody and the body's base on the behavior of the lee-side wake of pointed slender bodies at high angles of attack has not been thoroughly studied.

Serdaroglu *et al.* [31] investigated experimentally the effects of the forebody geometry on the asymmetric side forces by measuring surface pressure along the body but only the mean pressure was measured. Degani and Zilliac [9] used a long ogive-cylinder body ($L/D = 16$) and measured high frequencies of the flow at angles of attack up to $\alpha = 80^\circ$. Zilliac *et al.* [10], using a similar body configuration ($L/D = 16$), tested the effect of small perturbations placed at the tip of the forebody on the unstable wake at angles of attack up to $\alpha = 80^\circ$; smoke visualization and velocity measurements indicated multivortex pairs in the wake.

Kumar and Prasad [25] reported experiments and computations of an ogive-cylinder configuration of $L/D = 16$ when a ring is placed around the ogive-cylinder junction. By changing the height of the ring the total side forces could be altered. Computations at $\alpha = 50^\circ$ demonstrated a multivortex structure at the lee side but no unsteadiness was reported. Kumar and Prasad [32], using the model and flow conditions as in Kumar and Prasad [25], reported that with the increase in the

angle of attack, the number of vortices in the multivortex system also increases. Kumar [20] with the configuration of Ref. [25] observed that the rolling moment of the body also increased with the increase of the angle of attack. Qi *et al.* [26] performed wind tunnel experiments and numerical simulations with a 13.8$D$ long ogive-cylinder with a flat base to show at $\alpha = 50^\circ$ that bistable asymmetric flow structures were present when a small disturbance was placed at circumferential locations around the body tip; the corresponding side forces acting on the slender body were shown as square waves (similar to previously published studies, e.g., Zilliac *et al.* [10], Degani and Tobak [11], Degani [33], Gendel *et al.* [34]). No details were reported on how the base was numerically treated.

The current study investigates the development of nonstationary side forces along an inclined ogive-cylindrical body with a sharp tip and a blunt base for angles of attack ranging from 20° to 80°, with specific attention to the influence of the tip, the base, and the afterbody's length. The bifurcation diagrams of the side forces acting on the entire body are compared against the diagrams of its main components, namely, the ogive forebody and the cylindrical afterbody. For the analysis, the body is divided into a large number of narrow cross-section disks, and for each disk the time histories of rms and the mean of the side force acting on its surface are computed. The obtained sectional side-force distribution is studied against the resultant side forces of the forebody, the afterbody, and the full body. Three different body configurations are tested, using three different disturbances for each configuration. The body is subjected to three-dimensional, compressible, laminar flow with Reynolds number based on body diameter of 30 000 and Mach number of 0.2. The second-order implicit Beam-Warming finite-difference scheme is employed to solve the full, time-dependent Navier-Stokes equations.

## II. PROBLEM FORMULATION

This section includes a summary of the governing equations and the numerical algorithm that have been described in great detail in previously published papers [35–38], followed by a detailed description of algorithm validation and verification.

### A. Governing equations and numerical algorithm

The conservation equations of mass, momentum, and energy can be represented in a flux-vector form as

$$\partial_\tau \hat{Q} + \partial_\xi \hat{E} + \partial_\eta \hat{F} + \partial_\varsigma \hat{G} = \frac{1}{\mathrm{Re}}(\partial_\xi \hat{E}_\nu + \partial_\eta \hat{F}_\nu + \partial_\varsigma \hat{G}_\nu), \tag{1}$$

where $\tau$ is the dimensionless time, $\tau = a_\infty t/D$, $a_\infty$ is the free-stream speed of sound, and $D$ is the body diameter; $\mathrm{Re}_D = \rho_\infty U_\infty D/\mu_\infty$, where $U_\infty$ is the free-stream velocity, $\rho_\infty$ is the free-stream density, $\mu_\infty$ is free-stream viscosity. The independent spatial variables $\xi$, $\eta$, and $\varsigma$ are chosen to map a curvilinear body-conforming grid into a uniform computational space. In Eq. (1), $\hat{Q}$ is the vector of dependent flow variables; $\hat{E} = \hat{E}(\hat{Q})$, $\hat{F} = \hat{F}(\hat{Q})$, and $\hat{G} = \hat{G}(\hat{Q})$ are the inviscid flux vectors; and the terms $\hat{E}_\nu$, $\hat{F}_\nu$, and $\hat{G}_\nu$ are fluxes containing derivatives of the viscous terms. A dimensionless form of the equations [35] is used throughout this work. The characteristic length is the body diameter $D$ and all spatial parameters are made dimensionless in respect to it (e.g., $x/D$, $h/D$, $L/D$, etc.). The implicit Beam-Warming finite-difference algorithm [36], which is second-order accurate both in time and space [35,36], is adapted to solve Eq. (1) in a three-dimensional curvilinear coordinate system [38], where all viscous terms are retained [37].

Computations were performed for subsonic flows over an ogive-cylinder body of diameter $D$, which consists of a 3.5-diameter tangent-ogive forebody with several cylindrical afterbody lengths and a tangent 1:8 elliptic base [Fig. 1(a)]. An adiabatic no-slip boundary condition was applied at the body surface, at the circumferential edges of the grid an implicit periodic continuation condition was imposed and at the computational outer boundary undisturbed free-stream conditions were

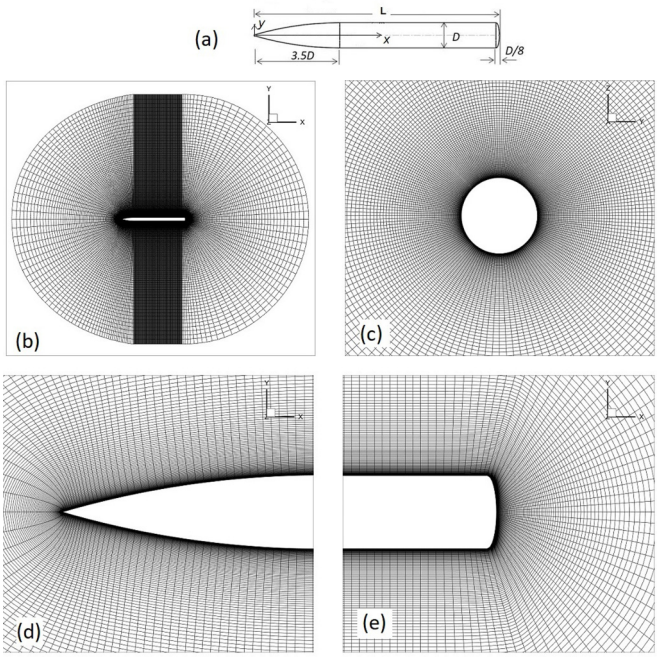


FIG. 1. Body and grid: (a) body dimensions, (b) $x$-$z$ plane of the entire grid, (c) $y$-$z$ cross section of the grid, (d) $x$-$z$ plane of symmetry of grid around the forebody, and (e) $x$-$z$ plane of symmetry of grid around body's aft.

maintained. The angle of attack $\alpha$ between the longitudinal axis ($x$) and the free-stream velocity ($\boldsymbol{U}_\infty$) was varied between 20° and 80°.

The grid [Fig. 1(b)] consists of 200 circumferential planes with uniform spacing of $\Delta\phi = 1.5°$ ($\phi$ is the circumferential direction and the leeward plane is at $\phi = 0°$) on the leeward side of the body and the rest of the planes are linearly stretched around the windward side with the largest $\Delta\phi = 2.96°$ at the windward ray [Fig. 1(c)]. In order to make the three-dimensional grid perfectly symmetric about the vertical plane, one side of the grid was generated by rotating the two-dimensional (2D) lee-side grid plane around one half of the body, and then it was mirror imaged to create the other half of the three-dimensional grid. In each circumferential plane, the grid contained 180 radial points between the body surface and the computational outer boundary at a radial distance of 40 body diameters, $D$. The largest spacing increment along the body surface in the longitudinal direction was $\Delta x = 0.105D$ which translates to 226 axial points between the tip [Fig. 1(d)] and the rear of the body [Fig. 1(e)] for the case with a body length of $L/D = 20$ (178 axial points for the $L/D = 15$ case and 130 axial points for the $L/D = 10$ case).

### B. Validation and verification

The computational code used in the current study has been extensively tested over the years by the author [22,23,28,34,37,39–41] and others (e.g., Refs. [42,43]) for flows and configurations identical or similar to the one considered in the current work. Other versions of the code were validated and verified by other researchers for numerous cases of more complex configurations (e.g., Refs. [44–48]). The code was tested with the current configuration (i.e., sharp forebody, slender body of revolution) for a wide range of flow conditions, subsonic as well as supersonic, laminar, and turbulent. Results had been checked against experimental data [8,9,14] and found to be very satisfactory [23,39,40].

TABLE I. Computations vs experiment [9] at $x/D = 6.6$.

| Case | Dimensionless time step | Dimensional time step (s) | Strouhal number $x/D = 6.6\ \alpha = 70^\circ$ | Strouhal number $x/D = 6.6\ \alpha = 80^\circ$ |
|---|---|---|---|---|
| (1) $140 \times 200 \times 120$ | 0.01 | $6.35 \times 10^{-7}$ | 0.145 | 0.162 |
| (2) $180 \times 200 \times 160$ | 0.01 | $6.35 \times 10^{-7}$ | 0.160 | 0.176 |
| (3) $226 \times 200 \times 180$ | 0.01 | $6.35 \times 10^{-7}$ | 0.163 | 0.178 |
| Experiment (Degani and Zilliac [9]) | | | 0.165 | 0.185 |

The Reynolds number of flow in the current work is $\mathrm{Re}_D = 30\,000$ and the flow is assumed to be laminar. This assumption is supported by numerous experimental and numerical studies; from the experiments we know that the flow around ogive-cylinder bodies at incidence is laminar even for Reynolds number (based on cylinder diameter) as high as 200 000. Lamont [8] separated the results of his experiments into three flow classes based on the separation type, namely, laminar, transitional, or turbulent. Lamont observed that for $\mathrm{Re}_D = 200\,000$, and below, the separation bubble and the reattachment were all laminar, and the flow at this regime was almost independent of angle of attack even at an angle as high as $\alpha = 90^\circ$. He also observed that for $\mathrm{Re}_D = 400\,000$, the separation bubble was laminar but the reattachment might be turbulent. While primary separation for the laminar cases is located circumferentially approximately as early as 85 ° from the windward ray, for the fully turbulent cases its location is 110 °. Results of an experiment [10] where pressure-transducer measurements and smoke visualization taken at $\mathrm{Re}_D = 30\,000$ showed that the flow separation was laminar and the line of separation was located approximately 90° from the windward plane. Degani *et al.* [49] used oil flow technique in their experiment where photographs of surface flow patterns were taken; the ogive-cylinder body was $16D$ long, the Reynolds number was $\mathrm{Re}_D = 26\,000$, and angles of attack ranged from $\alpha = 30^\circ$ to $\alpha = 85^\circ$. The photographs show that the primary separation lines are at about 90° from the windward plane of symmetry, which indicates that the separation is laminar. Experiments of Wardlaw and Yanta [50], at $\mathrm{Re}_D = 150\,000$ using a blunt ogive-cylindrical configuration at angle of attack of $\alpha = 45^\circ$, and Dexter [51] at $\mathrm{Re}_D = 100\,000$ using three different forebodies at angles of attack in the range of $25^\circ \leqslant \alpha \leqslant 90^\circ$, also reported that the separations were laminar at those Reynolds numbers. Degani and Zilliac [9] using a tangent-ogive-cylinder body of $x/D = 16$ and for Reynolds numbers based on diameter 17 000, 26 000, and 35 000, found, using a pressure transducer, that the near-wake power-spectra characteristics were laminar even at angles of attack as high as 85 °. Laminar computations [23] (using a flux-vector splitting [52] algorithm to solve the thin-layer approximated Navier-Stokes equations) at $\mathrm{Re}_D = 200\,000$ matched the surface pressure of Lamont's measurements [8], including the location of the primary separation and reattachment. Nevertheless, even at the current low Re (30 000) the far wake would become turbulent; however, this part of the wake has a negligible effect on the pressure field near the body and, as a result, on the forces acting on it.

In order to further validate the code and the grid for the intended tasks, an additional unsteady test was conducted. The case chosen was the experiment of Degani and Zilliac [9] where the flow around a $3.5D$ ogive-cylinder body at high angles of attack was studied. The goal was to match the Strouhal number of the surface-pressure spectra at $x/D = 6.6$ for two angles of attack ($\alpha = 70^\circ, \alpha = 80^\circ$) and Reynolds number based on cylinder diameter of $\mathrm{Re}_D = 35\,000$. Three grids were tested, $140 \times 200 \times 120$, $180 \times 200 \times 160$, and $226 \times 200 \times 180$ (axial $\times$ circumferential $\times$ radial); the dimensionless time step for the computations was $\Delta\tau = 0.01$ (this is equivalent in the experiment configuration, see [9], to $\Delta t = 6.3 \times 10^{-7}$ s; $\Delta\tau = a_\infty \Delta t/D$, $a_\infty = 340$ m/s, $D = 0.0216$ m). For each angle-of-attack case, sufficiently long runs were made and the Strouhal numbers of the oscillating side-force coefficients at $x/D = 6.6$ were calculated. Table I summarizes the results.

Both the second and third grids, above, show good agreement with the experimental data. Nevertheless, the largest grid ($226 \times 200 \times 180$) was chosen for the current study.

## III. RESULTS

All computations presented here were carried out by solving the full three-dimensional Navier-Stokes equations for the following flow parameters: free-stream Mach number $M_\infty = 0.2$ and Reynolds number $\mathrm{Re}_D = 30\,000$. For all calculations a dimensionless time step of $\Delta\tau = 0.01$ was used (this is equivalent to $5.9 \times 10^{-7}$ s in this study's flow conditions and body diameter of $D = 0.02$ meter).

A small disturbance of a triangle wedge shape was placed near the tip and its height in all cases was set to $h/D = 0.004$, its base to $b/D = 0.002$, and its length $\ell/D = 0.01$. For each angle of attack at least three different disturbance locations were calculated, at circumferential angle $\Phi \sim 2^\circ$ off the leeward plane of symmetry; at $\Phi = 90^\circ$, i.e., perpendicular to the leeward plane of symmetry; and at $\Phi \sim 174^\circ$ ($6^\circ$ off the windward plane of symmetry). As demonstrated in numerous experimental [2,10,11,13,19,25,32] and computational [17,22,23,24,33,39,40] studies the particular shape of the disturbance is not important as long as its size is small enough so that the actual force inflicted on it by the flow is insignificant in comparison to its global effect.

### A. Full body

Figure 2 shows a sample of results of the time histories (left) and power spectra (right) of side-force coefficient Cy exerted by the flow on the entire body (here of $L/D = 20$) at several angles of attack with the disturbance at circumferential angle $\Phi = 90^\circ$ (the side-force coefficient is defined as $C_Y = F_Y/(0.5\rho_\infty U_\infty^2 S)$, where $F_Y$ is the total side force acting on the body, $\rho_\infty$ is the free-stream density, $U_\infty$ is the free-stream velocity, and $S$ is the model base area). The dimensionless Strouhal

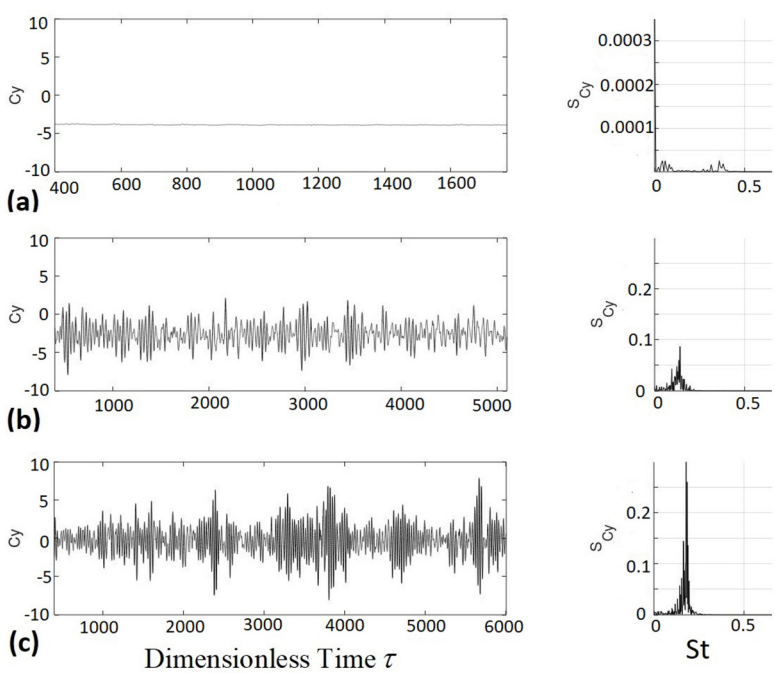


FIG. 2. Time histories (left) and power spectra (right) of side-force coefficient Cy of a full body: (a) $\alpha = 40^\circ$, (b) $\alpha = 50^\circ$, and (c) $\alpha = 80^\circ$. $L/D = 20$, $\Phi = 90^\circ$.

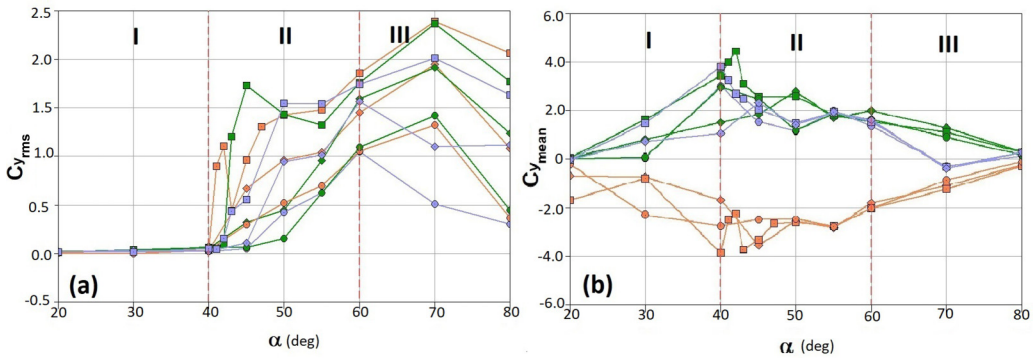


FIG. 3. Bifurcation diagrams for (a) root mean square of the side force coefficients, and (b) the mean of the side-force coefficients, as functions of the angle of attack. Symbols: circles: $L/D = 10$; diamonds: $L/D = 15$; squares: $L/D = 20$. Symbol colors: gray, disturbance at $\Phi = 2^\circ$ from leeward plane of symmetry; orange, $\Phi = 90^\circ$; green, $\Phi = 174^\circ$. The diagram is divided into three regions: I: steady, II: transitional, and III: nonstationary.

frequency is $\mathrm{St} = fD/U_\infty$, where $f$ is the frequency of the time-history signal of Cy; $S_{\mathrm{Cy}}$ is the power spectra of the time-history signal.

At $\alpha = 40^\circ$ the time history of the side force Cy shows that the flow is steady with some very low amplitude nonstationary oscillations due to the wake at the base [28]. At the higher angles of attack [Figs. 2(b) and 2(c)] the time history of the side force is nonstationary with large amplitude oscillations and with distinct Strouhal frequencies of Cy ($\mathrm{St} = 0.14$ at $\alpha = 50^\circ$, and $\mathrm{St} = 0.185$ at $\alpha = 80^\circ$).

From the time history of the resultant side-force coefficient exerted by the flow on the body, the mean ($\mathrm{Cy}_{\mathrm{mean}}$) and the root mean square ($\mathrm{Cy}_{\mathrm{rms}}$) are calculated, where

$$\mathrm{Cy}_{\mathrm{mean}} = \frac{1}{n}\sum_i \mathrm{Cy}_i, \tag{2}$$

$$\mathrm{Cy}_{\mathrm{rms}} = \sqrt{\frac{1}{n}\sum_i \mathrm{Cy}_i^2}, \tag{3}$$

and $n$ is the number of measurements.

### *1. Bifurcation diagrams—full body*

Figure 3 portrays the mean [Fig. 3(a)] and the root mean square [Fig. 3(b)] of the resultant side-force coefficient exerted by the flow on the body for cases where the body is held fixed at different angles of attack. Three body lengths are used, and each length is marked by a different symbol: circles for $L/D = 10$, diamonds for $L/D = 15$, and squares for $L/D = 20$. For each angle of attack, three different disturbance locations are calculated; each location is marked by a different color: green for a disturbance at circumferential angle $\Phi = 174^\circ$ from the leeward plan of symmetry, orange for $\Phi = 90^\circ$, and gray for $\Phi = 2^\circ$. Since the solutions are nonstationary, each case was run long enough to obtain meaningful mean values and rms of the oscillation amplitudes of Cy. Note that some of the symbols may be overlapped. The symbols of each body length are connected by colored lines to help separate the results but have no physical meaning.

The diagram can be divided into three regions: I: where solutions are steady (rms of Cy is zero or close to zero) for $\alpha \leqslant 40^\circ$; II: transitional region in the range $40^\circ < \alpha < 60^\circ$; and III:non-stationary solutions region for $\alpha \geqslant 60^\circ$. From Fig. 3(a) it is clear that in regions II and III the $\mathrm{Cy}_{\mathrm{rms}}$ of the longer body (squares, $L/D = 20$) is larger than $\mathrm{Cy}_{\mathrm{rms}}$ of the other two (with some variation

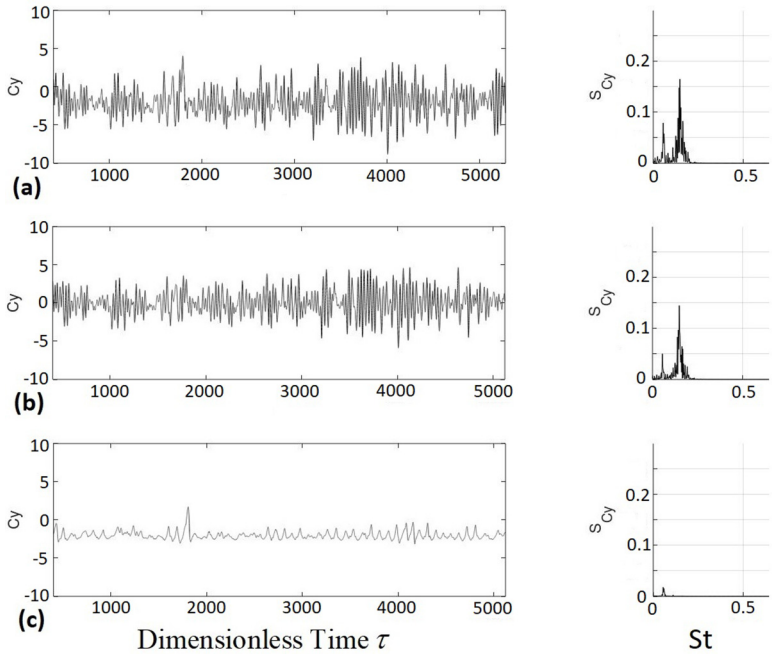


FIG. 4. Time histories (left) and power spectra (right) of side-force coefficient, Cy: (a) full body, (b) cylindrical afterbody, and (c) tangent-ogive forebody. $\alpha = 60^\circ$, $L/D = 20$, disturbance at $\Phi = 90^\circ$.

depending on the location of disturbances) with maximum value at $\alpha = 70^\circ$. The $\mathrm{Cy}_{\mathrm{rms}}$ of the medium body (diamonds, $L/D = 15$) is larger than $\mathrm{Cy}_{\mathrm{rms}}$ of the short ($L/D = 10$, circles) one. On the other hand, the mean of Cy does not show any significant difference for the different body lengths. $\mathrm{Cy}_{\mathrm{mean}}$ increases monotonically with the increasing angle of attack, reaches its maximum at $\alpha = 40^\circ$, and decreases monotonically for the higher angles.

### B. Forebody vs afterbody

In practical usage (e.g., flow-structure interaction) the body as a whole is usually considered; therefore, calculating the total Cy of the entire body is justified. However, from the standpoint of understanding the physics of the flow around the body, the total Cy can be misleading. A natural step is to analyze the effect of the flow around the $3.5D$ ogive forebody separately from the flow around the cylindrical afterbody. Figure 4 shows the time history of side-force coefficien Cy (left) and their power spectra (right) at angle of attack of $\alpha = 60^\circ$ with a disturbance at $\Phi = 90^\circ$ from the leeward plane of symmetry.

Figure 4(a) presents the entire body, Fig. 4(b) is for the cylindrical afterbody, and Fig. 4(c) is for the ogive forebody. By comparing Figs. 4(a)–4(c), it becomes clear that the contribution of the ogive forebody to the unsteadiness of the side force is minimal; however, its contribution to the mean Cy is significant (the mean Cy of the cylindrical afterbody is almost zero and the large mean Cy of the full body is due to the contribution of the forebody). The forebody's dominant Strouhal frequency is $\mathrm{St} = 0.05$. The afterbody's dominant frequency is $\mathrm{St} = 0.17$; the secondary peak is the frequency due to the forebody's frequency. The full body's dominant frequencies are similar to those obtained for the afterbody.

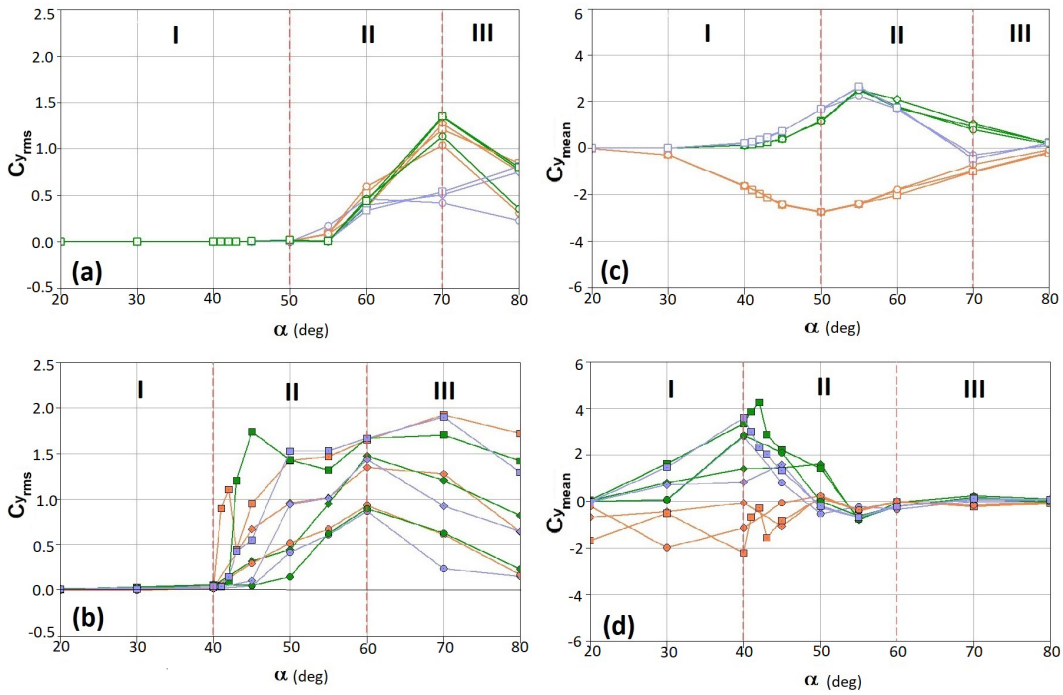


FIG. 5. Bifurcation diagrams: (a) $Cy_{rms}$ of the ogive forebody, (b) $Cy_{rms}$ of the cylindrical afterbody, (c) $Cy_{mean}$ of the ogive forebody, and (d) $Cy_{mean}$ of the cylindrical afterbody. Symbols: circles: $L/D = 10$; diamonds: $L/D = 15$; squares: $L/D = 20$. Open symbols: ogive forebody; full symbols: cylindrical afterbody. Symbol colors: gray, disturbance at $\Phi = 2^\circ$ from leeward plane of symmetry; orange, $\Phi = 90^\circ$; green, $\Phi = 174^\circ$.

### *1. Bifurcation diagram—forebody and afterbody*

Similar to what was done for the full body, Fig. 5 presents the bifurcation diagrams of the mean and the root mean square of the side-force coefficients exerted by the flow. However, here we separate the side-force coefficients of the tangent-ogive forebody from the side-force coefficients of the cylindrical afterbody. Again, for every angle of attack three different body lengths (circles: $L/D = 10$; diamonds: $L/D = 15$; and squares: $L/D = 20$) and three disturbance locations (colored green for a disturbance at $\Phi = 174^\circ$ from the leeward plan of symmetry, orange for $\Phi = 90^\circ$, and gray for $\Phi = 2^\circ$) are calculated.

Figure 5(a) is the bifurcation diagram of the rms of the side-force coefficients of the ogive forebody (open symbols) and Fig. 5(b) is for the cylindrical afterbody (full symbols). It is apparent that the flow over the forebody behaves differently than the flow over the afterbody. The flow around the forebody at angles of attack up to $\alpha = 50^\circ$ (region I), is steady ($Cy_{rms} = 0$), asymmetric (Cy_mean $\neq 0$), and not sensitive to the cylindrical afterbody length. The transitional region of the ogive forebody [region II, Fig. 5(a)] is within $50^\circ < \alpha < 70^\circ$ (while steady solutions are obtained for $\alpha \leqslant 50^\circ$ and nonstationary solutions for $\alpha \geqslant 70^\circ$). On the other hand, the transitional region of the cylindrical afterbody [Fig. 5(b)] is within $40^\circ < \alpha < 60^\circ$, while steady solutions are obtained for $\alpha \leqslant 40^\circ$ and nonstationary solutions for $\alpha > 55^\circ$. $Cy_{rms}$ of the forebody does not show any significant difference for the different body lengths. However, it is clear that in regions II and III of the afterbody the $Cy_{rms}$ of the longer body (square symbols, $L/D = 20$) is larger than $Cy_{rms}$ of the other two (with some variation depending on the location of the disturbance) with maximum value at $\alpha = 70^\circ$. The $Cy_{rms}$ of the medium body (diamond symbols, $L/D = 15$) is larger than $Cy_{rms}$ of

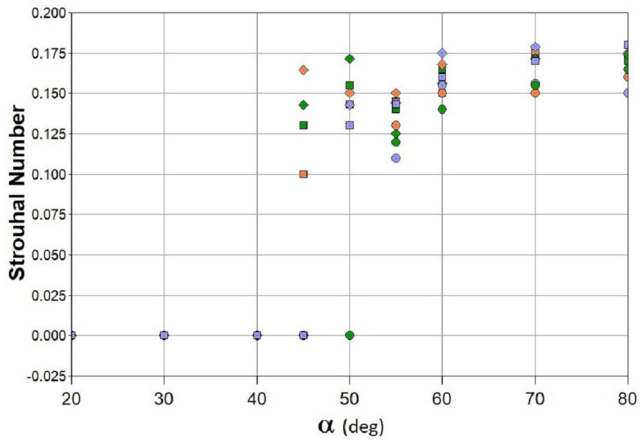


FIG. 6. Strouhal number of the wake at the lee side of the cylindrical afterbody as a function of angle of attack. Symbols: circles: $L/D = 10$; diamonds: $L/D = 15$; squares: $L/D = 20$. Symbol colors: gray, disturbance at $\Phi = 2^\circ$ from leeward plane of symmetry; orange, $\Phi = 90^\circ$; green, $\Phi = 174^\circ$.

the short one ($L/D = 10$, circle symbols). By comparing Fig. 5(b) with Fig. 3(a) it is noticeable that the separation between the results of the different body lengths is better defined owing to the fact that $\mathrm{Cy}_{\mathrm{rms}}$ of the forebody is eliminated.

Another significant difference between the forebody and the afterbody is the behavior of the mean Cy with angles of attack. The mean Cy of the ogive forebody [Fig. 5(c)] increases monotonically with the increasing angle of attack, reaches its maximum at $\alpha = 50^\circ \sim 55^\circ$ (depending on disturbance location), and decreases monotonically at the higher angles with little effect of body length (this means, therefore, that the afterbody has little influence on the flow around the forebody). However, the mean Cy of the cylindrical afterbody [Fig. 5(d)] reaches its maximum at $\alpha \sim 40^\circ$ and diminishes rapidly, for all three body lengths, for angles of attack larger than 55 °, meaning that the nonstationary flow around the cylindrical afterbody is virtually symmetric at angles of attack larger than 55 °. This also means that at these high angles of attack the exclusive source of the side-force asymmetry is the flow around the forebody. When the total side force acting on the entire body is calculated, this important characteristic is masked.

#### *2. Strouhal Number of lee-side wake*

Figure 6 presents the Strouhal number of the dominant frequency of the lee-side wake of the cylindrical afterbody as a function of the angle of attack. In all cases, for angles of attack lower than 45 ° no shedding occurs and the Strouhal number is $\mathrm{St} = 0$, and for angles of attack above $55^\circ$ the Strouhal number flattens out at a value a bit lower than the expected Strouhal number for a 2D cylinder ($\mathrm{St} = 0.2$); The range of $40^\circ < \alpha < 60^\circ$ is transitional. The results of the short body ($L/D = 10$) fall consistently below those of the two longer bodies (of $L/D = 15$ and $L/D = 20$).

### C. Sectional side force

At low Mach numbers, the pressure over the body surface changes smoothly and therefore the forces acting on the body surface change smoothly as well; therefore, to compute the sectional side forces along the body, the body is divided into $\sim 0.2D$-wide disks and at every time step of the numerical computation the side-force coefficient Cy acting on each disk's surface is computed separately (since the grid spacing along the body is not uniform, a disk's width is not necessarily exactly $0.2D$; however, the exact width of each disk is used in the calculation).

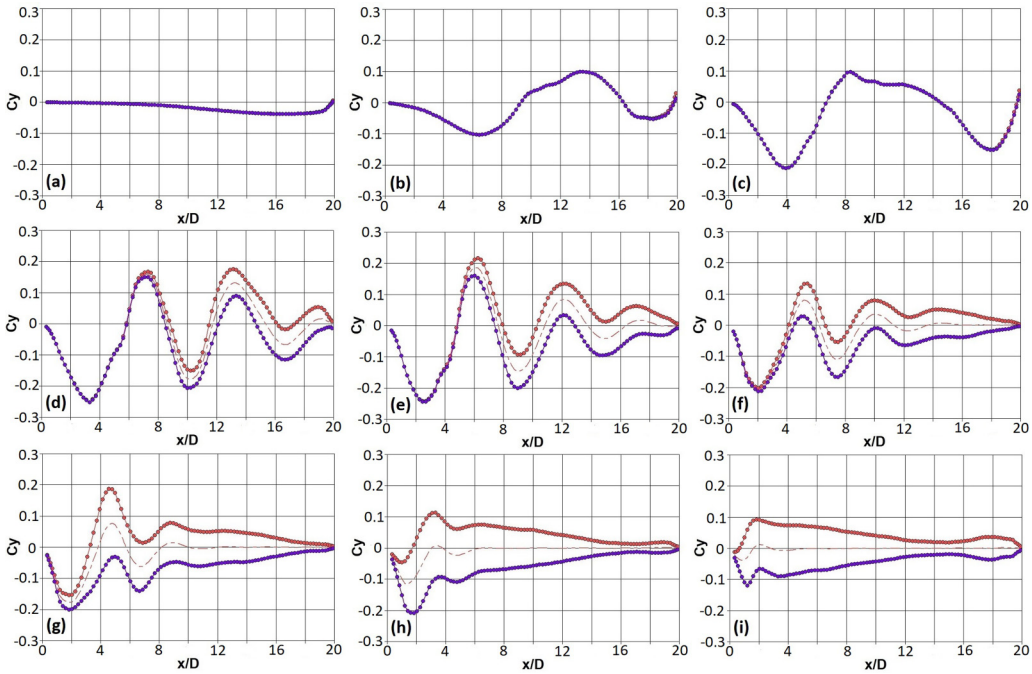


FIG. 7. Sectional side force (mean and rms) along the body: (a) $\alpha = 20^\circ$, (b) $\alpha = 30^\circ$, (c) $\alpha = 40^\circ$, (d) $\alpha = 45^\circ$, (e) $\alpha = 50^\circ$ (f) $\alpha = 55^\circ$, (g) $\alpha = 60^\circ$, (h) $\alpha = 70^\circ$, and (i) $\alpha = 80^\circ$. $L/D = 20$; one disturbance (at $\Phi = 90^\circ$) is used. Red circles are (mean + rms), dash-dotted line is mean, and purple circles are (mean–rms).

### *1. Unsteadiness and the effect of angle of attack*

From the time histories at each slice along the body, the Mean and the rms of the side-force coefficients Cy are calculated. Figure 7 shows the changes of the sectional side force along the body (for a body of $L/D = 20$ and a disturbance placed at $\Phi = 90^\circ$) at different angles of attack. The dash-dotted lines represent the mean of Cy at each cross section, the red circles are the (mean + rms), and the purple circles are the (mean–rms); this means that the flow is steady where the line of $\mathrm{Cy}_{\mathrm{mean}}$ and the two symbols coincide.

At low to moderate angles of attack the sectional side force along the entire body is steady, e.g., Fig. 7(a), $\alpha = 20^\circ$. At the higher end of this region, some small fluctuations may appear near the end of the body due to the influence of the unsteady wake at the base, e.g., Figs. 7(b) and 7(c), $\alpha = 30^\circ$ and $\alpha = 40^\circ$, respectively, where at $x/D > 16$ the sectional side force shows some unsteadiness. However, in the transition region (in this study $40^\circ < \alpha < 55^\circ$), along a significant portion of the body, the sectional side force shows large-amplitude oscillations [e.g., Fig. 7(d), $\alpha = 45^\circ$; Fig. 7(e), $\alpha = 50^\circ$], while the mean of the sectional side force shows large asymmetry caused by the steady asymmetric tip vortices (and maybe due to more steady vortex pairs emanating from the body surface). The extent of the waviness of Cy along the body depends on the proximity and the spatial position of the off-surface vortices near the body surface. The explanation for the coexistence of the large-amplitude oscillations and the large mean asymmetry may come from Fig. 8. This is a set of *helicity density* [53] snapshots at cross section $x/D = 15$ of the $\alpha = 50^\circ$ case presented in Fig. 7(e) (helicity density is defined as the scalar product of the local velocity and vorticity vectors; it indicates both the strength and sense of rotation of the vortices). The two red and blue blobs at the top of each snapshot are the cross sections of the tip vortices. These asymmetric vortices are stationary, as can be seen from the snapshots, and they are the cause of the large asymmetry of the side force. Below them are the nonstationary vortices which are shed from the body. They are

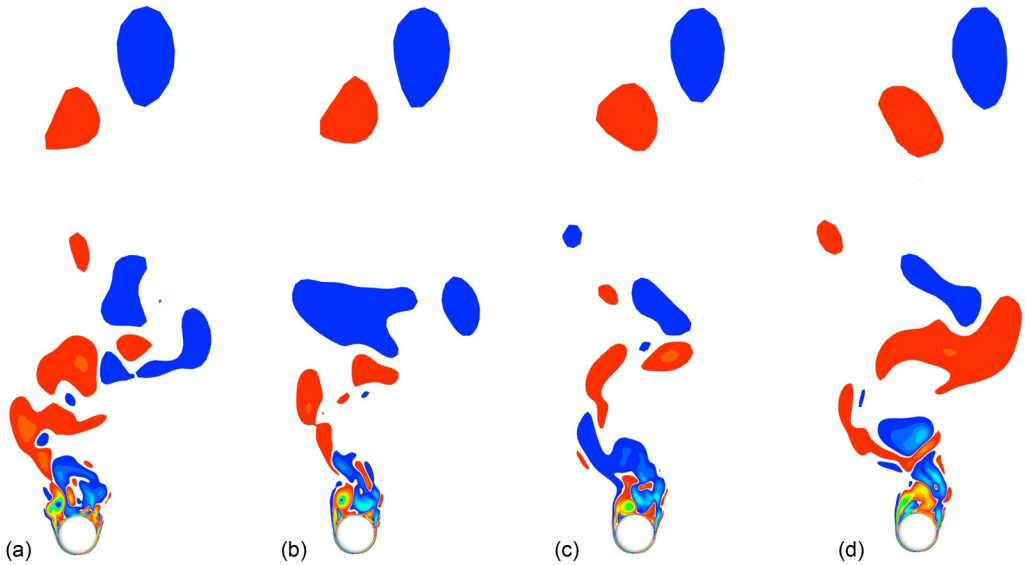


FIG. 8. Stationary vs nonstationary vortices; one-cycle snapshots of helicity-density contours at cross section $x/D = 15$: (a) $t = 0$, (b) $t = T/4$, (c) $t = T/2$, and (d) $t = 3T/4$. $T = 1/f = 0.0275$, $\alpha = 50^\circ$, and disturbance at $\Phi = 90^\circ$.

the cause of the large-amplitude oscillations. The frequency which is used to determine the cycle $T$ for the snapshots is the frequency of the dominant signal of the oscillating side force at this cross section, $f = 0.0275$ (or $\mathrm{St} = 0.1375$).

As the angle of attack increases the unsteady region extends more and more toward the tip of the body. Also, with increasing angle of attack, the wave shape of the sectional $\mathrm{Cy}_{\mathrm{mean}}$ along the body becomes more pronounced. The maximum peak to peak of this waviness is at $\alpha = 50^\circ$ [Fig. 7(e)] and decreases at higher angles of attack. At the end of the transition region, $\alpha = 55^\circ$ [Fig. 7(f)], the oscillations of the sectional side-force coefficient along the aft of the body ($x/D > 15$) become symmetric and $\mathrm{Cy}_{\mathrm{mean}}$ diminishes; in addition, only along a small portion of the forebody ($x/D < 2$) is the sectional side force steady ($\mathrm{Cy}_{\mathrm{rms}}$ is zero). In the unsteady region ($\alpha > 55^\circ$) the sectional side force along the entire body is unsteady ($\mathrm{Cy}_{\mathrm{rms}} > 0$); in this region, as the angle of attack increases, the portion of the body's aft where Cy oscillates symmetrically ($\mathrm{Cy}_{\mathrm{mean}} = 0$ ) extends further upstream [Figs. 7(g)–7(i)]. These symmetric oscillations are due to the classical von Kármán vortex shedding. Approaching 80 °, the symmetric oscillations cover almost the entire length of the body and the asymmetric tip vortices have very little influence on the side force.

### 2. *Effect of disturbance location*

Figure 9 presents the effect of the disturbance's location on the sectional side-force coefficients (while other parameters are kept unchanged) for two angles of attack: $\alpha = 30^\circ$ and $\alpha = 60^\circ$. The dash-dotted lines represent the mean of Cy and the circles (connected by solid lines) are the (mean + rms) and the (mean–rms); each color represents a different disturbance's location (gray circles for the disturbance at $\Phi = 2^\circ$, orange circles for the disturbance at $\Phi = 90^\circ$, and green circles for the disturbance at $\Phi = 174^\circ$). At $\alpha = 30^\circ$ [Fig. 9(a)] the flow of all three solutions is steady (with some small oscillations at the end of the body, caused by the nonstationary wake at the base). Two of the three locations cause almost the same side-force distribution even though these locations are opposite to each other ($\Phi = 2^\circ$ and $\Phi = 174^\circ$) and the green circles overlap the gray ones. There is no indication of hysteresis; e.g., if one starts from a steady solution, for example, from the one created with a disturbance at $\Phi = 90^\circ$, but now with a disturbance at $\Phi = 2^\circ$, the new solution

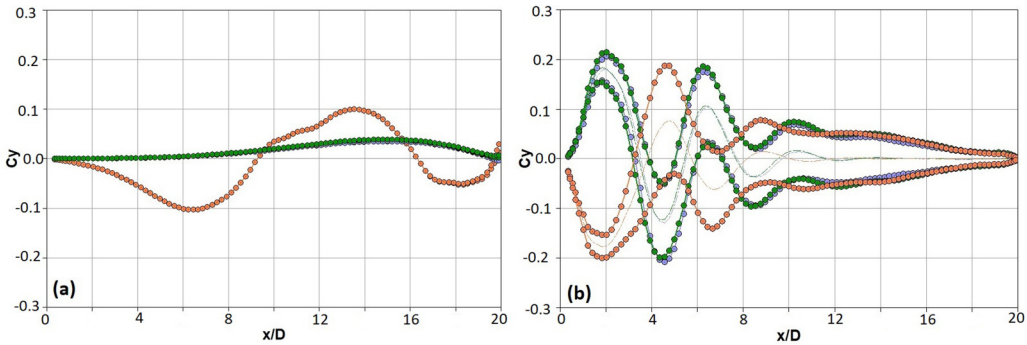


FIG. 9. Sectional side force (mean and rms) along the body for three different disturbances (gray circles, $\Phi = 2^\circ$; orange circles, disturbance at $\Phi = 90^\circ$; green circles, $\Phi = 174^\circ$); $L/D = 20$. (a) $\alpha = 30^\circ$ and (b) $\alpha = 60^\circ$.

would converge to the same solution that was obtained by starting from free stream and a disturbance at $\Phi = 2^\circ$. Starting from a steady solution which is obtained by using two disturbances, for example, one at $\Phi = 90^\circ$ and the other at $\Phi = 2^\circ$, and then one of the disturbances is removed, say, the one at $\Phi = 90^\circ$, the solution would converge to the same steady solution which was obtained with one disturbance at $\Phi = 2^\circ$ and starting from free stream. These results are consistent with the presence of a convective instability mechanism [11,21,44].

At higher angles of attack, here as a demonstration at $\alpha = 60^\circ$ [Fig. 9(b)], the flow is unsteady along the entire body. As in the previous demonstration for the lower angle of attack, the side-force coefficient distributions obtained for disturbances at $\Phi = 2^\circ$ and $\Phi = 174^\circ$ are almost the same. On the other hand, the solution for a disturbance at $\Phi = 90^\circ$ is almost a mirror image of the other two. In all three cases, the sectional $\mathrm{Cy}_{\mathrm{mean}}$ shows large asymmetry along the body up to $x/D = 10$ but for $x/D > 12$ all three solutions are almost identical and the oscillations have zero mean. As also shown earlier [Figs. 7(g)–7(i)] this behavior repeats itself at higher angles of attack: The oscillations of Cy along the afterbody have zero mean and the solutions of the three disturbances overlap each other's. This is the region of the classical von Kármán vortex shedding and the instability of the flow is global (or absolute [44,54]); this means that once a solution is established, changing the disturbance location does not change the solution at that area (here for $x/D > 12$). On the other hand, the region upstream of the global instability region is highly influenced by the stationary tip vortices (which causes large asymmetry and waviness of the sectional $\mathrm{Cy}_{\mathrm{mean}}$). As in the previous case of the moderate angle of attack, $\alpha = 30^\circ$, in this upstream region no hysteresis can be observed and the flow is convectively unstable (i.e., changing the disturbance location would change the sectional $\mathrm{Cy}_{\mathrm{mean}}$ along the body but it returns to its previous distribution if the location of the disturbance is reversed). This behavior at large angles of attack supports the hypothesis that two different phenomena are involved, namely, the convective behavior of the steady component of Cy caused by the stationary tip vortices and the absolute instability of the nonstationary vortex shedding from the cylindrical afterbody [44,54].

### *3. Effect of afterbody length*

Figure 10 demonstrates the influence of the afterbody length on the behavior of the sectional side force along the body. Three body lengths are presented ($L/D = 10$, 15, 20), and in all cases, the disturbance is located at $\Phi = 90^\circ$. The dash-dotted lines represent the sectional $\mathrm{Cy}_{\mathrm{mean}}$ and the two symbols of the same color are the (mean + rms) and the (mean–rms) and each color represents a different body length, $L/D$ (green circles, $L/D = 10$, gray circles, $L/D = 15$, orange circles, $L/D = 20$). As demonstrated earlier (e.g., Fig. 7), at $\alpha \leqslant 40^\circ$ the flow is steady along the entire body (except maybe near the body base where the unsteady wake at the base induces some small-amplitude

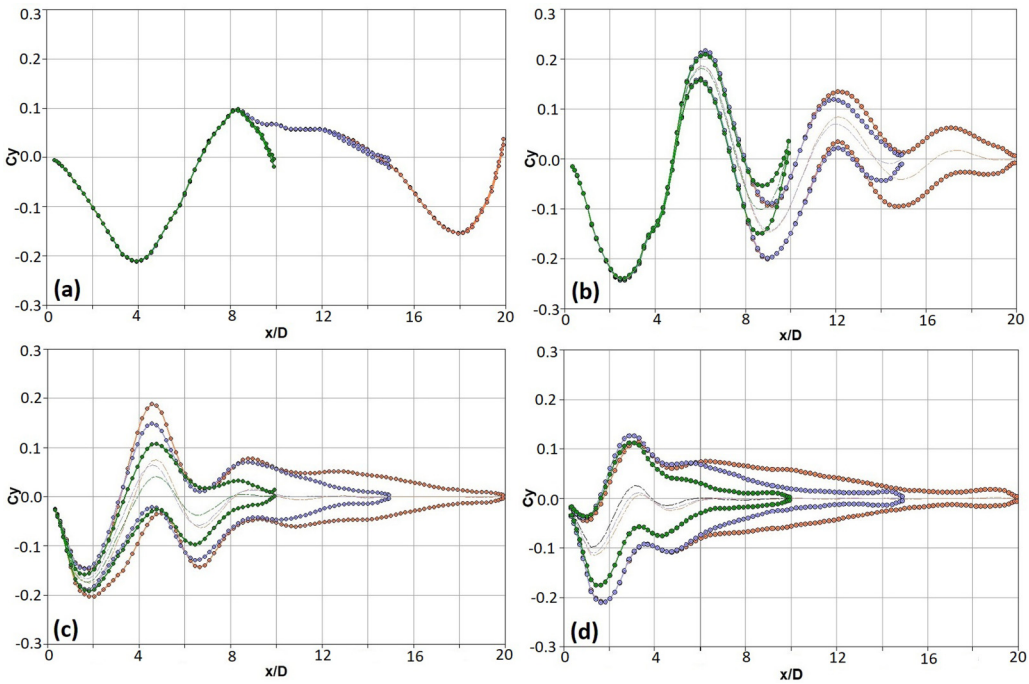


FIG. 10. Sectional side force along the body for different body lengths (green circles, $L/D = 10$; gray circles, $L/D = 15$; orange circles, $L/D = 20$); disturbance at $\Phi = 90^\circ$. (a) $\alpha = 40^\circ$, (b) $\alpha = 50^\circ$, (c) $\alpha = 60^\circ$, and (d) $\alpha = 70^\circ$.

oscillations of Cy), and the line of $\mathrm{Cy}_{\mathrm{mean}}$ and the symbols coincide. As can be seen in Fig. 10(a), this is true for all three body lengths. Moreover, from Fig. 10(a) it is clear that from the tip of the body up to $x/D = 8$ the sectional side-force coefficients for all three lengths are virtually the same (less than 2.5% difference). Beyond $x/D = 8$ the sectional side-force coefficients of the short body of $L/D = 10$ start to deviate due to the effect of the body base wake. The sectional side force of the medium body length $L/D = 15$ starts to deviate from the solution $L/D = 20$ case at about $x/D = 12$ (2.5% difference at this point). At $\alpha = 50^\circ$, [Figure 10(b)], the Kármán vortex shedding occurs along a large portion of the cylindrical afterbody but the effect of the tip vortices is also significant (causing the large waviness of the sectional Cy along the body). The region of oscillations extends further upstream (starting at about $x/D = 5$) and the rms of Cy further downstream is significant. Nevertheless, in the region where the flow is steady, from the tip and up to $x/D = 5$, the sectional side-force coefficients of all three lengths are virtually the same. Between $x/D = 5$ and $x/D = 8$ the sectional side-force coefficients of the short body of $L/D = 10$ show some deviation from those of the other body length cases and only for $x/D > 8$ is the deviation significant. The sectional side-force coefficients of the medium length of $L/D = 15$ start to deviate from those of the $L/D = 20$ case at about $x/D = 8$ and show a significant deviation for $x/D > 11$. At $\alpha = 60^\circ$ [Fig. 10(c)] the sectional side-force coefficients of the three different body lengths coincide only for a very short part of the forebody (less than $1.0D$ from the tip) where the flow is steady. Along the rest of the body's length, the rms of Cy is very large due to a massive von Kármán shedding. The mean sectional Cy along the entire $L/D = 10$ body is asymmetric. However, the flow at the aft of the longer bodies oscillates symmetrically and Cy has zero mean. At the higher angles of attack this behavior is even more pronounced. At $\alpha = 70^\circ$ [Fig. 10(d)] the wake along the entire body oscillates and the tip vortices have less influence and cause asymmetry only from the tip to about $x/D = 6$. As the body becomes longer the region of symmetric oscillations of Cy around zero mean also increases and

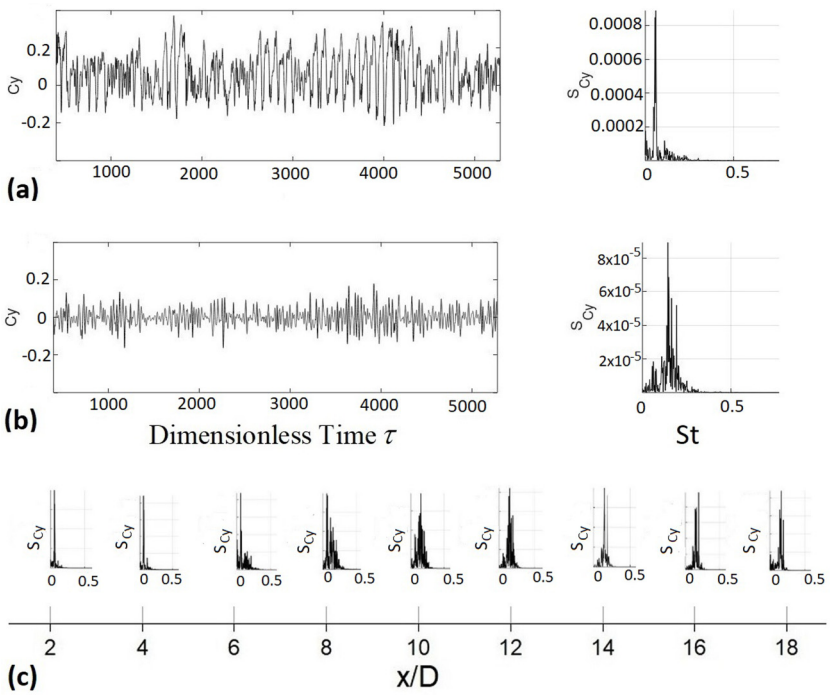


FIG. 11. Power spectra at angle of attack $\alpha = 60^\circ$; $L/D = 20$, disturbance at $\Phi = 90^\circ$. (a) Time histories (left) and power spectra (right) of sectional side-force coefficient Cy at $x/D = 4.5$. (b) Time histories (left) and power spectra (right) of sectional side-force coefficient Cy at $x/D = 14$. (c) Power spectra along the body.

covers a significant portion of the body. This means that at those high angles of attack increasing the body length beyond the point where the oscillations have zero mean changes the mean of the *total side force* very little. It also should be noted that as the body gets longer the oscillations amplitude of the sectional Cy also increases. The results of the other cases of disturbance locations (not shown, $\Phi = 2^\circ$, $\Phi = 174^\circ$) demonstrate the same behavior as observed for the disturbance at $\Phi = 90^\circ$ (Fig. 10).

#### *4. Power spectra along the body*

As demonstrated above, the amplitudes of the sectional side-force coefficients change along the body. Apparently, the frequencies change as well, as shown in Fig. 11 for the case of the long body, $L/D = 20$, at $\alpha = 60^\circ$ and disturbance at $\Phi = 90^\circ$. Figure 11(a) presents the time history (left) and power spectra (right) at $x/D = 4.5$ where the asymmetry and amplitude are the largest; the dominant Strouhal frequency is about $\mathrm{St} = 0.05$.

However, at $x/D = 14$ [Fig. 11(b)], which is at the middle of the cylindrical afterbody, the oscillations have smaller amplitudes with zero mean, and the power spectra is wide banded with a dominant Strouhal frequency $\mathrm{St} = 0.17$ (in both cases the signal is recorded over one grid cell). Figure 11(c) shows the change of power spectra at different stations along the body. The data for each plot are taken over a $1D$-wide section. Up to $x/D = 6$ the Strouhal frequency of the dominant signal is about $\mathrm{St} = 0.056$, and it grows to about $\mathrm{St} = 0.17$ for $x/D > 12$. The transition from the low Strouhal frequency to the high one occurs in the range $6 < x/D < 12$ and it can be identified by the wide-banded frequencies around the dominant one. The region of $x/D > 12$ is the region where the sectional $\mathrm{Cy}_{\mathrm{mean}}$ is almost zero and the classical von Kármán vortex shedding dominates. At the

higher angle of attack of $\alpha = 80^\circ$ (not shown) the frequency of the dominant signal at $x/D = 18$ is $\mathrm{St} = 0.19$, which is in good agreement with the experimental finding [9] ($\mathrm{St} \sim 0.2$).

### *5. Variation of the sectional* $\mathbf{Cy_{rms}}$ *and* $\mathbf{Cy_{mean}}$ *along the body*

Figure 12 summarizes the investigation of the sectional side-force bifurcation structure by comparing results of two body lengths and two disturbance locations. Figure 12(a) presents the rms of Cy of the long body ($L/D = 20$) with a disturbance at $\Phi = 90^\circ$ and Fig. 12(b) presents the sectional $\mathrm{Cy_{mean}}$ of this configuration. Along the forebody the flow becomes unsteady at angles of attack larger than $\alpha = 50^\circ$ (the results along the forebody are marked in green; the different symbols represent different $x/D$ locations). The largest amplitude of $\mathrm{Cy_{rms}}$ is at $x/D = 2$ and angle of attack $\alpha = 70^\circ$. The sectional $\mathrm{Cy_{mean}}$ of the forebody reaches its largest (absolute) value at $\alpha = 45^\circ$, just before the flow becomes unsteady. Along the afterbody the flow becomes unsteady at angles of attack larger than $\alpha = 40^\circ$ (the results along the afterbody are marked in orange). The largest $\mathrm{Cy_{rms}}$ along the afterbody is about 50% of the maximum value of $\mathrm{Cy_{rms}}$ along the forebody. The sectional $\mathrm{Cy_{mean}}$ along the afterbody reaches its largest (absolute) value also at $\alpha = 45^\circ$ and diminishes for angles of attack larger than $\alpha = 55^\circ$ (as the nonstationary oscillations of Cy become symmetric). The transitional region lies roughly along $4 < x/D < 8$ and is represented by the purple line of the cross section $x/D = 6$. The diagrams for the shorter body of $L/D = 15$ (and disturbance at $\Phi = 90^\circ$), Figs. 12(c) and 12(d), agree well with the results of the longer body of $L/D = 20$, Figs. 12(a) and 12(b), with somewhat lower values of $\mathrm{Cy_{rms}}$. At low angles of attack where the flow is steady along the entire body ($\alpha < 45^\circ$) the two bodies have practically the same bifurcation structure of the sectional side-force coefficients. This agreement is enhanced by flow visualization as portrayed in Fig. 13; Fig. 13(a) shows the helicity-density cross sections along the body and the traces of massless particles which are released near the core of the vortices of the $L/D = 20$ body at an angle of attack of $\alpha = 40^\circ$ and a disturbance at $\Phi = 90^\circ$. Two pairs of steady vortices are visible: the tip vortices and a second, steady, vortex pair which has not departed yet along the afterbody. Figure 13(b) shows results for the shorter body of $L/D = 15$ and the qualitative agreement with Fig. 13(a) is excellent.

Figures 12(e) and 12(f) are the $\mathrm{Cy_{rms}}$ and $\mathrm{Cy_{mean}}$, respectively, for $L/D = 20$ and the disturbance at $\Phi = 2^\circ$; Figs.12(g) and 12(h) are the $\mathrm{Cy_{rms}}$ and $\mathrm{Cy_{mean}}$, respectively, for $L/D = 15$ and $\Phi = 2^\circ$. The behavior of the results of those cases is similar to the cases with the disturbance at $\Phi = 90^\circ$ with the exception of a delay of the unsteadiness onset of the forebody which happens now at a higher angle of attack ($\alpha > 55^\circ$) and the maximum of $\mathrm{Cy_{rms}}$ along the forebody is lower than those of the previous case of disturbance at $\Phi = 90^\circ$. Here, again, the bifurcation diagram of the short body case $L/D = 15$ [Figs. 12(g) and 12(h)] matches well with the one of $L/D = 20$ (with some deterioration toward the end of the short body), as it is also evident from the helicity-density visualization and the massless particle traces [Figs. 13(c) and 13(d) vs Figs. 13(a) and 13(b)]. It should be noted that the position of the tip vortices in the $\Phi = 2^\circ$ case is a mirror image of those of $\Phi = 90^\circ$ (the left vortex is lower than the right one) and this is reflected by the opposite sign of $\mathrm{Cy_{mean}}$ diagrams of the two cases, even though the bifurcation diagrams of $\mathrm{Cy_{rms}}$ for both disturbance locations are very similar. One also should notice that in the $\Phi = 2^\circ$ case, a second steady pair of vortices departs from the body's surface (and at the aft of the longer body, a third pair starts), as it is clearly evident from Figs. 13(c) and 13(d), while in the $\Phi = 90^\circ$ cases these vortices have not lifted off yet from the lee side of the body.

## IV. CLOSING REMARKS

The current paper describes a numerical study of the evolution of nonstationary side forces along an ogive-cylinder body subjected to flows at a wide range of angles of attack from 20° to 80°. A second-order accurate implicit finite-difference scheme is employed for the flow equations, adapted to a three-dimensional curvilinear coordinate system. The flow is three-dimensional, compressible,

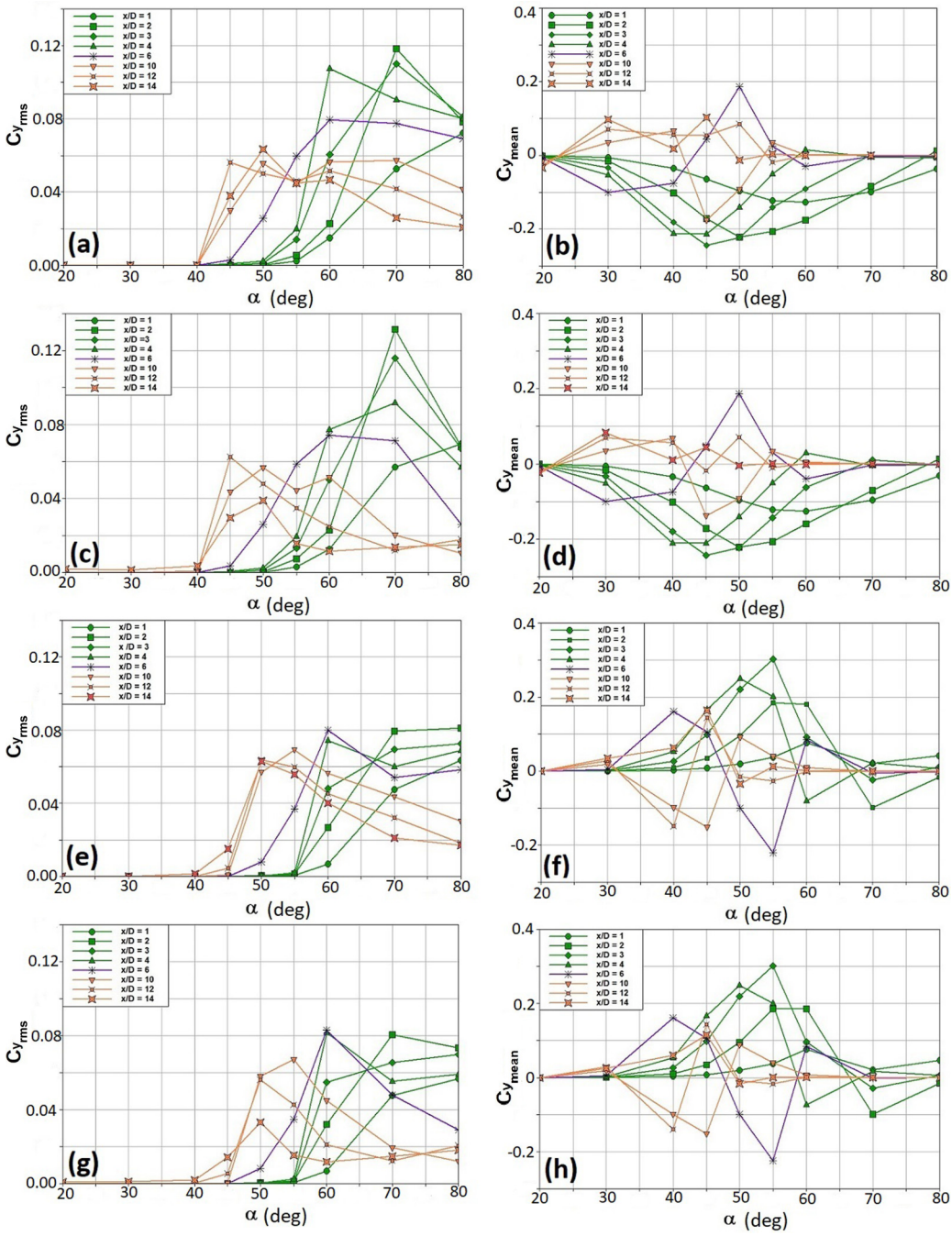


FIG. 12. Sectional side force bifurcation structure. (a) $Cy_{rms}$, $L/D = 20$, disturbance at $\Phi = 90^\circ$; (b) $Cy_{mean}$, $L/D = 20$, disturbance at $\Phi = 90^\circ$; (c) $Cy_{rms}$, $L/D = 15$, $\Phi = 90^\circ$; (d) $Cy_{mean}$, $L/D = 15$, $\Phi = 90^\circ$; (e) $Cy_{rms}$, $L/D = 20$, $\Phi = 2^\circ$; (f) $Cy_{mean}$, $L/D = 20$, $\Phi = 2^\circ$; (g) $Cy_{rms}$, $L/D = 15$, $\Phi = 2^\circ$; (h) $Cy_{mean}$, $L/D = 15$, $\Phi = 2^\circ$.

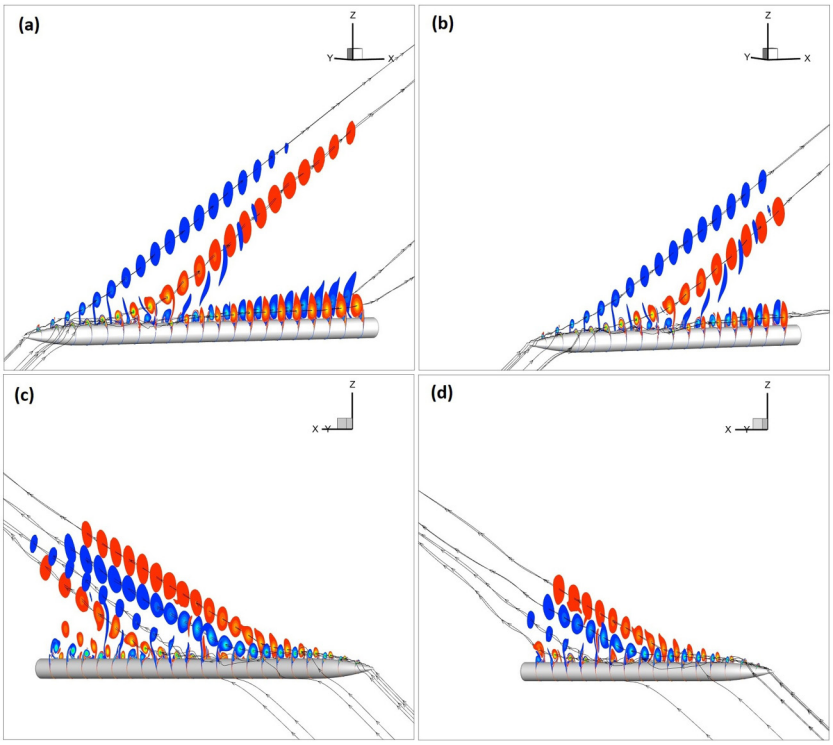


FIG. 13. Helicity density and particle traces, $\alpha = 40°$. (a) $L/D = 20$, disturbance at $\Phi = 90°$; (b) $L/D = 15$, $\Phi = 90°$; (c) $L/D = 20$, $\Phi = 2°$; (d) $L/D = 15$, $\Phi = 2°$.

and laminar; the Reynolds number is 30 000 based on the body diameter and the Mach number is 0.2. The ogive-cylinder body consists of a 3.5-diameter tangent-ogive forebody and three different cylindrical afterbodies with a blunt base are used; a small disturbance of a triangle wedge shape is placed near the tip and three different tip-disturbance locations are used, placed at a circumferential angle of $\Phi = 2°$, 90°, and 174° from the leeward plane of symmetry.

The present results show that the classical approach of using a single balance to measure the resultant side force of the entire body to determine the nature of the flow can be misleading. Separating the results of the forebody from those of the afterbody is a better approach. The bifurcation diagrams of the rms and the mean of Cy demonstrate significant differences between the flow around the 3.5$D$-ogive forebody and the flow around the cylindrical afterbody. By combining these diagrams (to form the full-body diagrams) the highly distinctive characteristics of the flow around the forebody and the flow around the afterbody are averaged out. The flow around the forebody at angles of attack up to $\alpha = 50°$ is steady ($\mathrm{Cy}_{\mathrm{rms}} = 0$) and asymmetric. Moreover, the $\mathrm{Cy}_{\mathrm{mean}}$ of the forebody at these angles of attack is not sensitive to the cylindrical afterbody length for all cases tested ($L/D = 10$, 15, and 20). On the other hand, the $\mathrm{Cy}_{\mathrm{mean}}$ diagram of the afterbody reveals that the nonstationary flow around the cylindrical afterbody is virtually symmetric for angles of attack above 55 °; this means that for those high angles of attack the existence of side-force asymmetry as measured on the full body is exclusively due to the flow around the forebody.

A better perspective of the flow field is revealed by computing sectional side-force coefficients along the body. Results demonstrate that at low or medium angles of attack (up to 40°) the flow is steady along the entire body except for some small oscillations near the body base at the higher end of the angle-of-attack range. As the angle of attack increases above 40°, the flow about the aft of the cylindrical afterbody becomes unsteady and this unsteady region extends more and more

toward the tip of the body as the angle of attack increases. When the angle of attack exceeds 50° the sectional side force Cy along the far aft of the body oscillates symmetrically with zero mean, and this symmetric region extends upstream with the increasing angle of attack until at $\alpha = 80°$ it covers almost the entire body. This means that at those high angles of attack (above 50°) increasing the body length beyond the point where the oscillations have zero mean changes the mean of the total side force very little. Changing the location of the tip disturbance at this range of angles of attack does not affect this symmetric region. This is the region where the instability of the flow is global (absolute). On the other hand, the region upstream of the global region is highly influenced by the departing *stationary* vortex pairs (which causes the large waviness of the sectional $\mathrm{Cy}_{\mathrm{mean}}$ along the body) and the flow is convectively unstable, meaning that changing the location of the tip disturbance changes the shape of the sectional $\mathrm{Cy}_{\mathrm{mean}}$ in this region but it returns to its original shape if the location of the disturbance is reversed. These results support the conjencture [44] that two different phenomena are involved, namely, the convective behavior of the steady component caused by the stationary tip vortices and the absolute instability caused by the nonstationary vortex shedding from the cylindrical afterbody.

Power-spectra analysis of the sectional side-force coefficients along the body at high angles of attack, where the wake on the lee side of the body is unsteady, shows that not just the Cy amplitude changes along the body but the frequency changes as well. The frequency of the dominant signal along the forebody is low and the power spectra is narrow banded. At the aft of the body where the mean Cy is almost zero, the classical von Kármán vortex shedding dominates, and as the angle of attack increases toward 90° the Strouhal number of the local Cy approaches the Strouhal number of the flow around a two-dimensional cylinder. The transition region from the low frequency of the forebody to the high frequency of the afterbody's aft can be identified by the wide-banded power spectra.

The bifurcation structures of the sectional $\mathrm{Cy}_{\mathrm{rms}}$ and $\mathrm{Cy}_{\mathrm{mean}}$ of the shorter body of $L/D = 15$ agree very well with the results of the longer body of $L/D = 20$, with somewhat lower values of $\mathrm{Cy}_{\mathrm{rms}}$ at angles of attack above 55°. At low angles of attack where the flow is steady along the entire body ($\alpha < 45°$) the two bodies have practically not only the same bifurcation structure of the sectional side-force coefficients but also the same off-surface vortex structure.

The data that support the findings of this study are available from the author upon reasonable request.

[1] J. H. Allen and E. W. Perkins, A study of effects of viscosity on flow over slender inclined bodies of revolution, NACA-TR-1048 (1951), ntrs.nasa.gov.

[2] W. Letko, A low-speed experimental study of the directional characteristics of a sharp-nosed fuselage through a large angle-of-attack range at zero angle of sideslip, NACA-TN-2911 (1953), ntrs.nasa.gov.

[3] F. E. Gowen and E. W. Perkins, A study of the effects of body shape on the vortex wakes of inclined bodies at a Mach number of 2, NACA Research Memorandum A53I17 (1953), ntrs.nasa.gov.

[4] F. E. Gowen and E. W. Perkins, Drag of circular cylinders for a wide range of Reynolds numbers and Mach numbers, NACA Technical Note 2960 (1953), ntrs.nasa.gov.

[5] L. H. Jorgensen and E. W. Perkins, Investigation of some wake vortex characteristics of an inclined ogive-cylinder body at Mach Number 1.98, NACA Research Memorandum A555E31 (1955), ntrs.nasa.gov.

[6] K. D. Thomson and D. F. Morrison, The spacing, position and strength of vortices in the wake of slender cylindrical bodies at large incidence, J. Fluid Mech. **50**, 751 (1971).

[7] P. J. Lamont and Hunt, Pressure and force distributions on a sharp-nosed circular cylinder at large angles of inclination to a uniform subsonic stream, J. Fluid Mech. **76**, 519 (1977).

[8] P. J. Lamont, Pressures around an inclined ogive cylinder with laminar, transitional, or turbulent separation, AIAA J. **20**, 1492 (1982).

[9] D. Degani and G. G. Zilliac, Experimental study of nonsteady asymmetric flow around an ogive-cylinder at Incidence, AIAA J. **28**, 642 (1990).
[10] G. G. Zilliac, D. Degani, and M. Tobak, Asymmetric vortices on a slender body of revolution, AIAA J. **29**, 667 (1991).
[11] D. Degani and M. Tobak, Experimental study of controlled tip disturbance effect on flow asymmetry, Phys. Fluids A **4**, 2825 (1992).
[12] S. E. Ramberg, The effects of yaw and finite length upon the vortex wakes of stationary and vibrating circular cylinders, J. Fluid Mech. **128**, 81 (1983).
[13] D. Degani and M. Tobak, Effect of upstream disturbance on flow asymmetry, in *AIAA Aerospace Sciences Meeting*, AIAA Paper 92-408 (AIAA, Reno, NV, 1992).
[14] P. J. Lamont, The complex asymmetric flow over a 3.5*d* ogive nose and cylindrical afterbody at high angles of attack, in *AIAA 20th Aerospace Sciences Meeting*, AIAA Paper 82-0053 (AIAA, Orlando, FL, 1982).
[15] P. C. Dexter and B. L. Hunt, The effects of roll angle on the flow over a slender body of revolution at high angle of attack, in *AIAA 19th Aerospace Sciences Meeting*, AIAA Paper 81-358 (AIAA, St. Louis, MO, 1981).
[16] B Ma, Y. Huang, and T. Liu, Low-frequency unsteadiness of vortex wakes over slender bodies at high angle of attack, Chin. J. Aeronaut. **27**, 772 (2014).
[17] B.-F. Ma and T. Liu, Low-frequency vortex oscillation around slender bodies at high angles-of-attack, Phys. Fluids **26**, 091701 (2014).
[18] R. L. Kruse, E. R. Keener, G. T. Chapman, and G. Claser, Investigation of the asymmetric aerodynamics of cylindrical bodies of revolution with variations in nose geometry and angles of attack to 58 ° and Mach numbers to 2, NASA Technical Memorandum 78533 (1979), ntrs.nasa.gov.
[19] C. A. Moskovitz, R. M. Hall, and F. R. Dejarnette, Effects of nose bluntness, roughness and surface perturbations on the asymmetric flow past slender bodies at large angles of attack, in *AIAA 7th Applied Aerodynamics Conference*, AIAA Paper 89-2236-CP (AIAA, Reston, VA, 1989).
[20] P. Kumar, Rolling moment of slender body at high incidence for air-to-air missile/rocket applications, Def. Sci. J. **70**, 18 (2020).
[21] K. B. Lua, T. T. Lim, and S. C. Luo, Helical-groove and circular-trip effects on side force, J. Aircr. **37**, 906 (2000).
[22] D. Degani and L. B. Schiff, Numerical simulation of the effect of spatial disturbances on vortex asymmetry, AIAA J. **29**, 344 (1991).
[23] D. Degani, Effect of geometrical disturbances on vortex asymmetry, AIAA J. **29**, 560 (1991).
[24] B.-F. Ma, Y. Huang, and X.-Y. Deng, Dynamic responses of asymmetric vortices over slender bodies to a rotating tip perturbation, Exp. Fluids **57**, 54 (2016).
[25] P. Kumar and J. K. Prasad, Effect of ring size on the side force over ogive-cylinder body at subsonic speed, Aeronaut. J. **120**, 1487 (2016).
[26] Z. Y. Qi, S. Y. Zong, and Y. K. Wang, Bi-stable asymmetry on a pointed-nosed slender body at a high angle of attack, J. Appl. Phys. **130**, 024703 (2021).
[27] Y. Zhu, H. Yuan, and C. Lee, Experimental investigations of the initial growth of flow asymmetries over a slender body of revolution at high angles of attack, Phys. Fluids **27**, 084103 (2015).
[28] M. Ishay, O. Gottlieb, and D. Degani, Computational fluid-structure interaction of a restrained ogive-cylindrical body with a blunt elliptical base at a high incidence, Phys. Rev. Fluids **6**, 014401 (2021).
[29] E. W. Perkins, Experimental investigation of the effects of support interference on the drag of bodies of revolution at a Mach number of 1.5, NACA Technical Note 2292 (1951), ntrs.nasa.gov.
[30] B. L. Hunt and P. C. Dexter, Pressures on a slender body at high angle of attack in a very low turbulence level airstream, in *AGARD Conference Proceedings No. 247*, High Angle of Attack Aerodynamics, Paper 17, AGARD-CP-247 (AGARD, Neuilly-sur-Seine, France, 1979).
[31] T. Serdaroglu, H. Pahlavani, and I. B. Ozdemir, Effects of forebody geometry on side forces on a cylindrical afterbody at high angles of attack, J. Aerosp. Eng. Mech. **4**, 177 (2020).
[32] P. Kumar and J. K. Prasad, Mechanism of side force generation and its alleviation over a slender body, J. Spacecr. Rockets **53**, 195 (2016).

[33] D. Degani, Instabilities of flows over bodies at large incidence, AIAA J. **30**, 94 (1992).
[34] S. Gendel, O. Gottlieb, and D. Degani, Fluid-structure interaction of an elastically mounted slender body at high incidence, AIAA J. **53**, 1309 (2015).
[35] T. H. Pulliam and J. L. Steger, Implicit finite-difference simulations of three-dimensional compressible flow, AIAA J. **18**, 159 (1980).
[36] R. M. Beam and R. F. Warming, An implicit factored scheme for the compressible Navier-Stokes equations, AIAA J. **16**, 393 (1978).
[37] D. Degani and S. W. Marcus, Thin vs. full Navier-Stokes computations for high angle-of-attack aerodynamics, AIAA J. **35**, 565 (1997).
[38] J. L. Steger, Implicit finite-difference simulation of flow about arbitrary two-dimensional geometries, AIAA J. **16**, 679 (1978).
[39] D. Degani, L. B. Schiff, and Y. Levy, Numerical prediction of subsonic, turbulent flows over bodies at large incidence, AIAA J. **29**, 2054 (1991).
[40] D. Degani and Y. Levy, Asymmetric turbulent flows over slender bodies, AIAA J. **30**, 2267 (1992).
[41] D. Degani, M. Ishay, and O. Gottlieb, Fluid-structure interaction of a rolling restrained body of revolution at high angles of attack, Phys. Fluids **29**, 037106 (2017).
[42] S. M. Murman, Geometric perturbations and asymmetric vortex shedding about slender pointed bodies, in *Atmospheric Flight Mechanics Conference*, AIAA Paper 2000-4103 (AIAA, Reston, VA, 2000).
[43] S. M. Murman, Vortex filtering for turbulence models applied to crossflow separation, in *39th Aerospace Sciences Meeting and Exhibit*, AIAA Paper 2001-0114 (AIAA, Reston, VA, 2001).
[44] L. B. Schiff, R. M. Cummings, R. L. Sorenson, and Y. Rizk, Numerical simulation of high-incidence flow over the F-18 fuselage forebody, J. Aircr. **28**, 609 (1991).
[45] N. M. Chaderjian, Comparison of two Navier-Stokes codes for simulating high-incidence vortical flow, J. Aircr. Rockets **30**, 357 (1993).
[46] R. E. Gordnier and M. R. Visbal, Unsteady vortex structure over a delta-wing, J. Aircr. **31**, 243 (1994).
[47] R. E. Gordnier and M. R. Visbal, Numerical simulation of delta-wing roll, Aerosp. Sci. Technol. **2**, 347 (1998).
[48] G. P. Guruswamy, Vortical flow computations on swept flexible wings using Navier-Stokes equations, AIAA J. **28**, 2077 (1990).
[49] D. Degani, M. Tobak, and G. G. Zilliac, Surface flow patterns on an ogive-cylinder at incidence, AIAA J. **30**, 272 (1992).
[50] A. B. Wardlaw and W. J. Yanta, Asymmetric flow field development on a slender body at high incidence, AIAA J. **22**, 242 (1984).
[51] P. Dexter, A study of asymmetric flow over slender bodies at high angles of attack in a low turbulence environment, in *22nd Aerospace Sciences Meeting*, AIAA Paper 84-505 (AIAA, Reno, NV, 1984).
[52] J. L. Steger and R. F. Warming, Flux vector splitting of the inviscid gasdynamic equations with applications to finite-difference methods, J. Comput. Phys. **40**, 263 (1981).
[53] Y. Levy, D. Degani, and A. Seginer, Graphical visualization of vortical flows by means of helicity, AIAA J. **28**, 1347 (1990).
[54] G. S. Triantafyllou, K. Kupfer, and A. Bers, Absolute Instabilities and Self-Sustained Oscillation in the Wakes of Circular Cylinder, Phys. Rev. Lett. **59**, 1914 (1987).